Functionalized p-silicon photocathodes for solar fuels applications: insights from Electrochemical Impedance Spectroscopy

Andrea Sartori,[a] Michele Orlandi,[a]* Serena Berardi,[b]* Alberto Mazzi,[a,c] Nicola Bazzanella,[a] Stefano Caramori,[b] Rita Boaretto,[b] Mirco Natali,[b] Rohan Fernandes,[d] Nainesh Patel,[d] Carlo Alberto Bignozzi,[b] Antonio Miotello.[a]

[a] Dipartimento di Fisica, Università degli Studi di Trento, Via Sommarive 18, 38123, Povo (Trento), Italy.
[b] Dipartimento di Scienze Chimiche e Farmaceutiche, Università degli Studi di Ferrara, Via Fossato di Mortara 17-19, 44121, Ferrara, Italy.
[c] Center for Materials and Microsystems, Fondazione Bruno Kessler, Via Sommarive 18, 38123, Povo (Trento), Italy.
[d] Department of Physics and National Centre for Nanosciences & Nanotechnology, University of Mumbai, Vidyanagari, Santacruz (E), Mumbai 400098, India.

* Contact author(s): michele.orlandi@unitn.it, serena.berardi@unife.it

Abstract. In this contribution we report on an in-depth electrochemical impedance spectroscopy (EIS) study of the interfaces and processes involved in the photoelectrochemical hydrogen production by efficient p-type silicon (pSi) photocathodes, designedly functionalized with protective and catalytic layers.
In particular, we have optimized the thermal evaporation of compact and conformal ultra-thin (5 nm) Ti films on pSi, with the double aim of (i) protecting the pSi surface from passivation and photocorrosion, as well as of (ii) introducing platforms with improved adhesion properties for the further functionalization with co-catalysts (in the specific, Pt nanoparticles). The best performing electrodes (labelled as pSi-5Ti-Pt) display an improved photocurrent onset (*ca.* 200 mV positive shift in 1 M H_2SO_4), as well as a more than doubled saturation photocurrent (up to -27 mA/cm^2) when compared to the unmodified pSi photocathodes. As evidenced by the EIS analysis, the proposed modifications of pSi surface led to an enhancement of the charge extraction from the semiconductor, most likely due to surface dipole effects able to reduce the resistance associated to the transport through the space charge layer. With respect to unmodified silicon, the presence of the Ti overlayer, partially oxidized to TiO_2, also allows for a denser surface coverage of the electrodeposited Pt nanoclusters, resulting in decreased interfacial charge transfer resistance for hydrogen evolution.
The proposed functionalization strategy relies on common fabrication methods (already applied at industrial level) and can be easily extended to other photoelectrode materials prone to passivation/photocorrosion and/or difficult to functionalize, thus introducing more flexibility in the choice of materials for photoelectrochemical cells.

Keywords: ultra-thin film, photocathode, electrochemical impedance spectroscopy, silicon, titanium

1. Introduction

Photoelectrochemical cell (PEC) technology is today one of the main candidates for solar fuels synthesis. The process, an application of the concept of artificial photosynthesis [1], consists in the conversion and storage of solar energy into the chemical bonds of high energy-density molecular species. Two of the most studied examples are H_2 from water splitting [2, 3] and, more recently, CO_2 reduction products (among them CO, CH_4, CH_3OH, CH_2O_2, CH_2O) [4-6]. The large-scale application of such technology has the potential to solve two important issues at the same time, *i.e.* to provide a method for storing intermittent sunlight while supplying cleaner fuels and/or high value-added products [7].

In its simplest design, a PEC device consists of an electrochemical cell with at least one photoactive electrode, where photon absorption leads to the separation of electrons and holes, which are then

available for redox reactions at the electrode/electrolyte interface. A commonly employed design, the tandem cell, requires the use of both a photoanode and a photocathode, thus offering the possibility to exploit separately optimized materials for absorbing different portions of the solar spectrum and performing either the anodic or the cathodic half-reaction [8]. In this framework, p-type silicon is a promising candidate as photocathode material, due to its optical band gap (1.12 eV) and conduction band edge energy, which makes it an excellent sunlight absorber (up to 1100 nm), thermodynamically capable of driving reduction reactions (*e.g.* hydrogen evolution and CO_2 reduction) [4, 9]. In addition, its earth-abundance, low-cost and scarce toxicity are all important pre-requisites for industrial scalability [10].

The main problems limiting the use of silicon are the prompt formation of insulating SiO_2 at the surface, even under (photo)cathodic conditions and in the presence of negligible amounts of oxygen, as well as its poor catalytic properties [11, 12]. Furthermore, only a relatively low photovoltage can arise from the semiconductor/electrolyte junction formed when p-type silicon (pSi) photocathodes are used in aqueous solution [13]. To circumvent all these problems, various strategies have been explored, including surface doping with emitting layers to maximize the attainable photovoltage [13, 14], the use of protective coatings [15, 16], and the functionalization with co-catalysts to boost the hydrogen evolution reaction [11, 17, 18], as well as combinations of them [13, 14].

Although the aforementioned strategies have been widely pursued, electrochemical impedance spectroscopy (EIS) studies of the charge transfer dynamics involved in H_2-generation by functionalized pSi photocathodes operating under illumination are still rare [19-22]. Thus, in this work we report on an in-depth EIS characterization of the interfaces formed by modification of flat pSi electrodes with an ultra-thin (5 nm) Ti protecting layer followed by decoration with catalytic Pt nanoparticles.

Photoelectrochemical characterization of the resulting Ti-Pt modified pSi photocathodes has revealed that the proposed functionalization led to enhanced performances in 1 M H_2SO_4, *i.e.* the doubling of the saturation photocurrent, and a 200 mV shift of the photocurrent onset with the respect to bare pSi. This is only partly due to the formation of an antireflective coating following Ti- and Pt- deposition. Indeed, Absorbed Photon to Current Efficiency (APCE) and EIS analyses point towards an improved charge-extraction and surface electrocatalysis from pSi as the main reason for this behaviour.

2. Experimental section

2.1 Fabrication of the Photoelectrodes

p-type Si substrates (PB-Technik AG, boron doped, Resistivity: 0.4-0.7 Ω·cm) were washed by sonicating in acetone and isopropanol for 5 minutes, then etched in HF (20%, 2 min) immediately before either photoelectrochemical characterization (in the case of bare pSi) or Ti- / Pt- deposition, in order to remove the native SiO_2.

Ultra-thin films of Ti were fabricated by using a custom-built Joule effect evaporator consisting of a vacuum chamber containing a spiral tungsten wire heating element and a substrate holder equipped with a calibrated quartz microbalance as thickness monitor. A metallic titanium (99.6%) foil was placed in contact with the heating element at a distance of 36 cm from the substrate holder. A baseline vacuum of $5x10^{-7}$ mbar was established before deposition. The deposition rate was maximized to limit possible in-flight oxidation. Pt nanoparticles (Pt-NPs) were electrodeposited on the surface of either pSi (to obtain pSi-Pt electrodes) or Ti-coated pSi (pSi-5Ti-Pt electrodes) from a degassed 1 mM solution of the H_2PtCl_6 precursor, at -0.15 V *vs* SCE for 10 minutes [23].

All the photocathodes were back contacted using silver conductive paste (Sigma Aldrich) and their active areas isolated using Kapton tape. For each electrode, the area exposed to the electrolyte was calculated, being usually in the range 0.5-0.8 cm^2.

2.2 Characterization of the Photoelectrodes

The morphology and elemental composition of the films were characterized by using a JEOL JSM-7001F FEG-SEM scanning electron microscopy (SEM) apparatus, equipped with an energy dispersive X-ray spectroscopy detector (EDXS, Oxford INCA PentaFETx3). Measurements were performed at 20.0 keV electron beam energy and maintaining the working distance between 3 and 8 mm. Surface morphology images were acquired in top-down and tilted modes, whereas cross-sectional analysis was performed putting the films on a 90° stub. Surface composition was analyzed by X-ray photoelectron spectroscopy (XPS) performed using a PHI 5000 VersaProbe II equipped with a monochromatic Al Kα (1486.6 eV) X-ray source and a hemispherical analyzer. Electrical charge compensation was required to perform the XPS analysis. No pre-sputtering was performed to avoid damaging the film. Reference binding energies (BE) are taken from the NIST X-ray Photoelectron Spectroscopy Database [24]. Atomic force microscopy (AFM) images were collected using a Digital Instruments Nanoscope III scanning probe Microscope (Digital Instruments, CA). The instrument was equipped with a silicon tip (RTESP-300 Bruker) and operated in tapping mode. Surface topographical analysis of raw AFM images was carried out with NanoScope analysis 1.5 program.

UV-Vis reflectance spectra were measured with a JASCO V-570 with a bandwidth of 2 nm equipped with an integrating sphere, and corrected for $BaSO_4$ spectrum as the 100% R background.

Photoelectrochemical measurements were carried out on a PGSTAT 30 electrochemical workstation in a three-electrode configuration, using SCE and Pt wire respectively as the reference and the counter electrode. A LOT-Oriel solar simulator, equipped with an AM1.5G filter, was used as the illumination source, and set to 0.1 W/cm^2 incident irradiance power by means of a Power Meter (Newport 1918-C). J-V curves, recorded at 20 mV/s scan rate, were repeated by cycling the photocathodes until an overlapping response upon subsequent scans (stationary state) was achieved. J-V curves under shuttered illumination were acquired by manually chopping the excitation source. Unless otherwise stated, all the potential values are given versus the saturated calomel reference electrode (SCE).

Incident Photon to Current Efficiencies (IPCEs) were measured in a three-electrode configuration under the monochromatic illumination generated by an air cooled Luxtel 175 W Xe lamp, coupled to an Applied Photophysics monochromator. The resulting photocurrent, recorded at the constant potential of -0.9 V, was measured by a PGSTAT 30 potentiostat. Absorbed Photon to Current Efficiencies (APCEs) were calculated from IPCE data corrected for the corresponding absorbed light values (*i.e.* the complementary values of the reflectance data, %A = 100 - %R).

Electrochemical Impedance Spectroscopy (EIS) in the dark was used to obtain the Mott-Schottky plots of the photocathodes. The electrodes were sampled from +0.2 to -0.6 V at 50 mV intervals employing a FRA2.v10 frequency response analyzer controlled by Nova 1.10. A 10 mV amplitude sinusoidal perturbation whose angular frequency ω ranged from 100000 and 100 Hz, was used (single-sine frequency scan mode for ω > 2.6 kHz and 5-sine frequency scan mode for ω < 2.6 kHz). In the EIS experiments under illumination, the photocathodes were instead sampled from -0.2 to -0.6 V at 100 mV intervals, employing the same instrumental set-up. A 10 mV amplitude sinusoidal perturbation, whose frequency ranged between 100000 and 0.1 Hz, was used (single-sine frequency scan mode for ω > 2.6 kHz and 5-sine frequency scan mode for ω < 2.6 kHz). The EIS data were fitted by means of the equivalent circuit reported in Scheme 1 using the ZView software, with typical relative errors lower than 10%. The Kronig-Kramers test (available as a tool in Nova 1.10) was performed on both the real and imaginary parts of all EIS data, obtaining χ^2 values (*i.e.* the

sum of squares of the relative residuals) of *ca.* $2 \div 7 \cdot 10^{-6}$ for the potential values corresponding to the steepest part of the J-V curves, and of *ca.* $1 \div 5 \cdot 10^{-5}$ (still considerable as data fit of reasonable quality) in the flat regions.

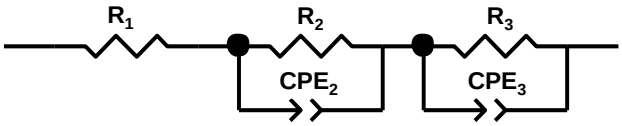

Scheme 1. Equivalent circuit used to fit the EIS data of the photocathodes.

In the circuit of Scheme 1, R_1 accounts for the ohmic resistance; R_2 is the charge transport resistance through the space charge layer of pSi and CPE_2 the corresponding constant phase element (non-ideal capacitance); R_3 is the charge transfer resistance of the photocathode/electrolyte interface and CPE_3 the corresponding constant phase element (non-ideal capacitance).

The hydrogen evolution experiments were carried out upon solar-simulated irradiation of a custom-made gas-tight reactor composed of two compartments separated by a frit. In the first compartment three ports are present, two of them are used for the working and the reference electrode while the third one is connected to a headspace from which automatic withdrawal by the GC pump takes place for gas detection and quantification. In the second compartment, one port is present and used for the counter electrode. All connections involving electrodes are gas-tight (Ace Glass Inc., USA). The gas atmosphere of the first compartment was analysed on an Agilent Technologies 490 microGC equipped with a 5 Å molecular sieve column (10 m), a thermal conductivity detector, and using Ar as carrier gas. 5 mL from the headspace are sampled by the internal GC pump and 200 nL are injected in the column maintained at 60°C for separation and detection of gases. The unused gas sample is then reintroduced in the reactor in order to minimize its consumption along the whole experiment. The Faradaic Efficiency (FE) of a sample is determined by comparison with the amount of hydrogen produced through a galvanostatic electrolysis (10 mA, 1 hour) of a 0.1 M H_2SO_4 solution in the same conditions using a Pt working electrode and assuming 100% FE.

3. Results and discussion.

As already mentioned above, flat pSi surfaces were firstly functionalized with ultra-thin metallic Ti layers, fulfilling the manifold roles of: (i) protecting the underlying silicon from passivation (provided that a conformal and pin-hole free coverage is formed), without blocking light absorption by the semiconductor; (ii) promoting charge separation *via* the resulting Schottky junction (a higher built-in potential is expected to form due to the lower work function of Ti with respect to silicon [16], as schematically depicted in Figure 1); (iii) constituting a platform for the further functionalization of the photocathodes with charge-transfer catalysts (in the specific case, Pt-NPs are considered).

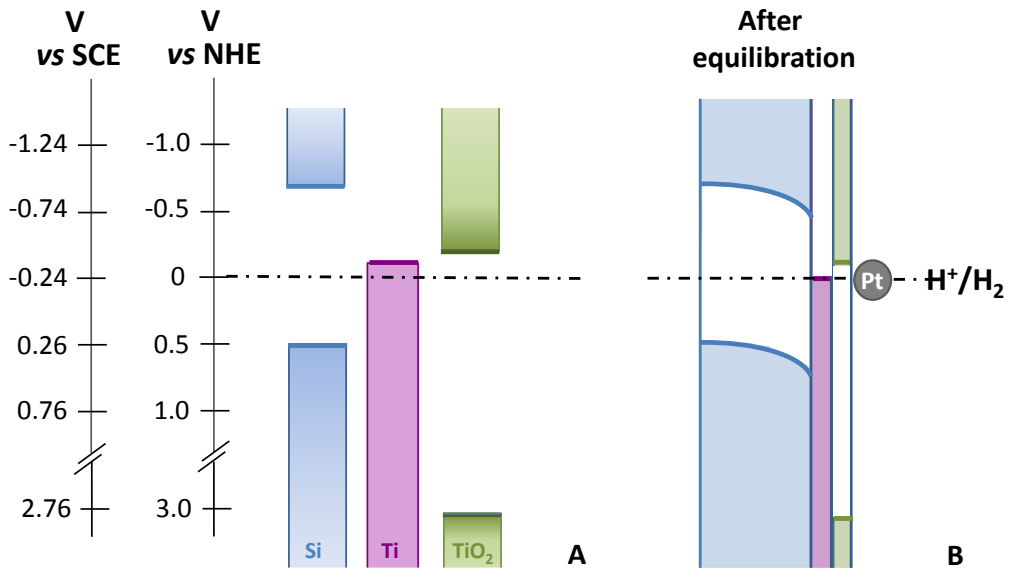

Figure 1. Schematic representation of the energy levels of the materials constituting the pSi-5Ti-Pt intefaces before (A) and after (B) the contact with the electrolye.

In particular, in our case the optimized thermal evaporation of metallic Ti results in the complete coverage of pSi surface with ultra-thin (5 nm) compact and conformal layers, as visible from the tilted mode SEM image reported in Figure 2a. Figure 2b shows the cross-section SEM for a 10 nm Ti film deposited in the same conditions (pSi-10Ti), where the denser film structure can be better appreciated.

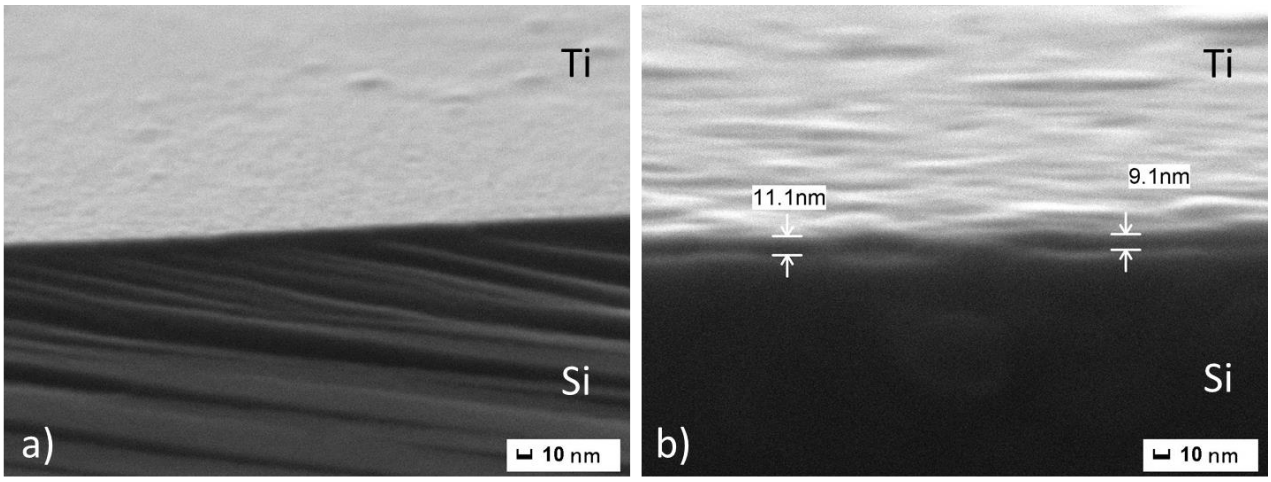

Figure 2. a) SEM image of pSi-5Ti, tilted mode; b) cross-section of pSi-10Ti.

While EDXS confirms the uniform presence of Ti and O along with Si, we employed XPS analysis to investigate the chemical composition of the film. The XPS spectrum reported in Figure 3a reveals the characteristic peaks of TiO_2 (Ti $2p_{3/2}$ BE = 458.5 eV; Ti $2p_{1/2}$ BE = 464.4 eV; O 1s BE = 530.0 eV), indicating the formation of the native oxide on the surface. Indeed, 3-5 nm thick TiO_2 layers were commonly found on metallic Ti films [15, 25, 26]. It is worth noting that the observed partial oxidation of Ti is not expected to jeopardize the performances of the resulting photoelectrodes, since TiO_2: (i) is transparent (> 3 eV band-gap); (ii) it has good electron conductivity; (iii) its conduction band edge is correctly aligned to facilitate

minority carrier transfer to the electrolyte (even though in our specific case the thickness of TiO_2 probably enables tunnelling, while also minimizing the voltage drop across the protecting layer); (iv) it is stable in a wide range of pHs [27]. Given all these properties, TiO_2 is indeed one of the most commonly used protective material for low band-gap photocathodes and photoanodes [16]. In addition, a closer look at the signal deconvolution of the Ti 2p region (Figure 3b) also shows the minor but distinct presence of residual metallic Ti (Ti $2p_{3/2}$ BE = 453.8 eV and Ti $2p_{1/2}$ BE = 460.0 eV) and possibly of Ti_2O_3 (Ti $2p_{3/2}$ BE = 457.0 eV and Ti $2p_{1/2}$ BE = 463.2 eV), indicating an incomplete conversion to TiO_2. These results are in agreement with a recent investigation of similar layers by high-resolution transmission electron microscopy [26]. For the sake of simplicity, the photoelectrodes will be further on indicated as pSi-5Ti, avoiding any explicit reference to the various surface phases formed as a consequence of surface oxidation. Another remarkable observation arising from Figure 3a is the absence of any signal due to the pSi substrate at 90° take-off angle, in agreement with the presence of a complete and conformal covering layer.

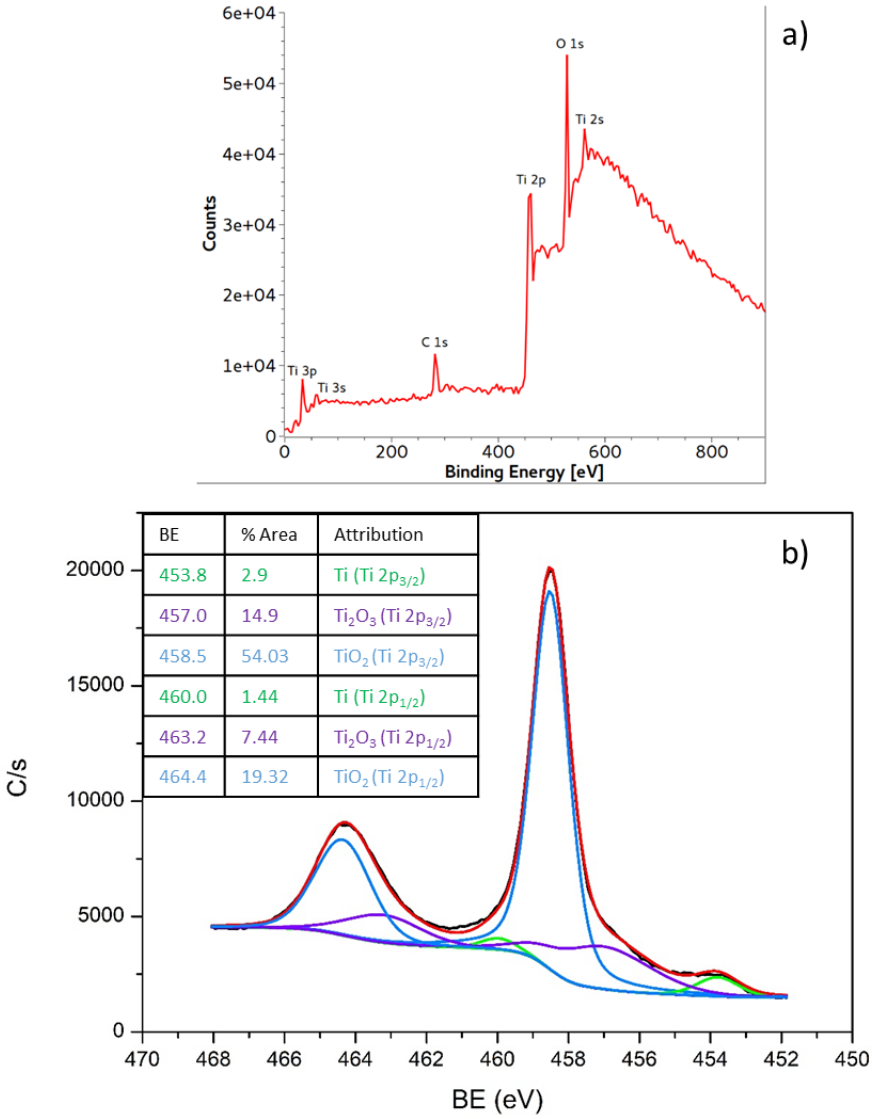

Figure 3. a) XPS spectrum of pSi-5Ti; b) Ti 2p region and peak deconvolution. In black is the XPS spectrum and in red the composite fit.

Figure 4a shows the photoelectrochemical characterization (current density *vs* potential, J-V curves) of all the prepared electrodes in degassed 1 M H_2SO_4, under 1 sun (0.1 W/cm^2) AM1.5G illumination. Each curve, recorded with iR drop compensation, is an average of 2-4 different electrodes, thus the corresponding sigmoidal fit is also reported for sake of clarity. The J-V curves recorded under shuttered illumination are also reported in Figure S1, evidencing the negligible dark contribution in the explored potential range for all the electrodes. The conformal Ti coverage of the pSi surface results in better performing electrodes, as clearly evidenced by the comparison with the bare electrodes (see blue *vs* black curves in Figure 4a). A doubling of the saturation current (up to -27 mA/cm^2 at -1 V), as well as a 100 mV shift of the photocathodic onset (given at J = -1 mA/cm^2) have been observed. A lower surface reflectivity (*ca.* 30% *vs* 45-50% for bare silicon, Figure S2) ensues from the deposition of the Ti layer, partly explaining the improved limiting photocurrent, but other effects related to an improved charge extraction from the pSi-Ti junction are present, as it will be further confirmed by EIS and APCE results (*vide infra*).

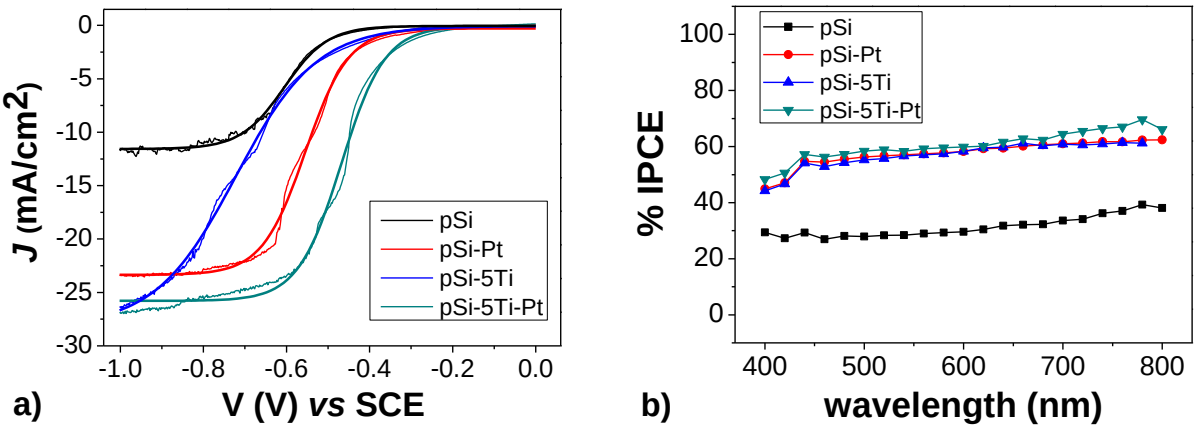

Figure 4. a) Photoelectrochemical performances of the prepared photocathodes in degassed 1 M H_2SO_4 under 1 sun (0.1 W/cm^2) AM1.5G illumination, corrected for the iR drop. Sigmoidal fits of the experimental averaged curves are also reported as thicker curves. b) IPCE photoaction spectra of the different photocathodes in degassed 1 M H_2SO_4 under -0.9 V applied bias.

Both pSi and pSi-5Ti electrode surfaces have been further functionalized by electrodepositing Pt-NPs, with the aim of: (i) improving the interface kinetics by boosting the proton reduction reaction; (ii) preserving sufficiently high light absorption by silicon; and (iii) investigating the suitability of the Ti layers as functionalization platforms. The presence of Pt-NPs on bare pSi results in a doubled saturation photocurrent (see black *vs* red curves in Figure 4a), as well as in a *ca.* 120 mV anodic shift of the onset potential (the low photovoltage value depends on the high work function of Pt, which is similar to that of pSi [28]). The presence of the Ti layer results in an improved onset shift for pSi-5Ti-Pt photocathodes with the respect to bare pSi (200 mV, see cyan *vs* black curves in Figure 4a), thus again confirming the better interfacial behavior of the protected electrodes. Furthermore, pSi-5Ti-Pt photocathodes reach up to -27 mA/cm^2 saturation photocurrents at -0.65 V. Their medium-term stability has been also assessed (Figure 5), showing that the saturation photocurrent value is retained for at least 5.5 hour irradiation under -0.9 V applied bias. The observed increase of the photocathodic current during the measure is probably ascribable to lensing effect by some H_2 bubbles that accumulate and stay stuck on the surface of the photoelectrode, until they finally detach. For sake of comparison, the photocathodic performances of the bare pSi tested under the same conditions are also reported. In this case, a similar initial improvement of the photocurrent is followed by its gradual decrease (*ca.* 20% less after 5.5 h), thus evidencing the need of a protective layer for the long-term operation of this kind of interfaces.

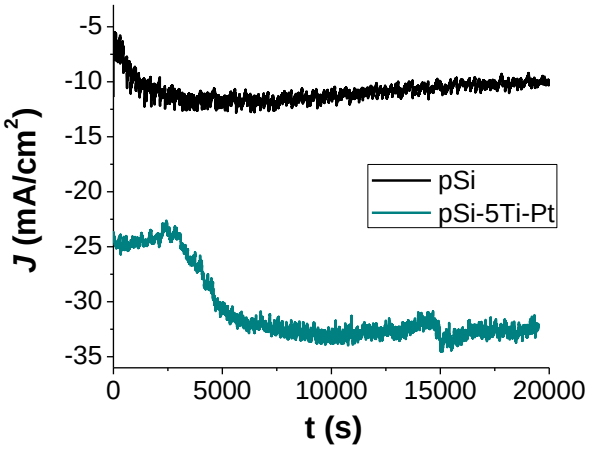

Figure 5. Chronoamperometries of pSi and pSi-5Ti-Pt photocathodes in degassed 1 M H_2SO_4 under -0.9 V applied bias and 1 sun (0.1 W/cm^2) AM1.5G illumination. Each curve is the averaged result of two experiments.

Experiments aimed at the quantification of the evolved hydrogen gas from both bare pSi and pSi-5Ti-Pt photocathodes have been also performed. Figure S3 evidences the superior performances of the functionalized pSi-5Ti-Pt electrode, producing (at lower potentials) almost 5 times more H_2 than pSi. The corresponding faradic efficiency results to be 78%. The non-quantitative yield can be due to several factors including: (i) the reduction of some O_2, produced at the counterelectrode and diffused through the frit separating the two compartments; (ii) the H_2 stuck at the electrode surface, which does not reach the headspace; (iii) the non-perfect sealing of the cell. A slightly lower faradic efficiency (73%) has been obtained for the unmodified pSi.

In order to assess any optical role of the Ti layer, photoaction spectra have been also collected. In particular, Figure 4b reports the averaged Incident Photon to Current Efficiencies spectra (IPCE *vs* wavelength), calculated under -0.9 V applied bias, showing that all electrodes absorb and convert light in the whole visible range (400-800 nm). Furthermore, the IPCE values match, as expected, the J-V trends, with the Ti- and/or Pt-functionalized photocathodes almost doubling (50-70% IPCE) the performances of the bare pSi in the explored range.[1] The observed trend is retained when considering the Absorbed Photon to Current Efficiency spectra (APCEs, in Figure S4), obtained by correcting the IPCE values for the absorptance of the different photocathodes (calculated from the reflectance spectra reported in Figure S2) indicating that a mere antireflection effect of the Ti-layer and/or of the Pt-NPs on the photoelectrochemical activity of the modified interfaces cannot be held entirely responsible for the observed results.

Thus, in order to better rationalize the properties of the interfaces involved in the photocurrent generation, we have performed EIS experiments on the different electrodes. The complex plane Nyquist plots, recorded under different applied biases (in the steepest region of the J-V curves), are reported in Figure S5 along with the corresponding fittings. All electrodes share similar impedance features, with two charge transfer arcs at high and low frequencies, respectively due to the resistances associated to the charge transport through the space charge layer (R_2 in Scheme 1), and to the interfacial charge transfer (R_3 in Scheme 1). Both these resistances decrease when increasing the applied bias towards negative values, as evidenced by

[1] The slight increase in the IPCE in the 700-800 nm range in the case of pSi and pSi-5Ti-Pt electrodes is probably just an artifact due to the difficult evaluation of the response factor in the red region of the visible spectrum with our experimental set-up, which also cannot analyse > 800 nm monochromatic wavelengths, thus preventing the IPCE to be measured up to the threshold of silicon band gap.

a shrinking of the associated semicircles (Figure S5). The corresponding R_1, R_2 and R_3 values, obtained from the abovementioned fittings, are reported in Table S1.

Figure 6 shows the inverse of the differential resistance (dI/dV, calculated from the I-V curves) versus the applied potential (gray curves), compared to R_2^{-1}, R_3^{-1} and R_{tot}^{-1} values (being $R_{tot} = R_1 + R_2 + R_3$ the total resistance). It can be clearly seen that R_{tot}^{-1} nicely correlates with the dI/dV curve in all cases, confirming that the selected circuital model properly describes the active elements involved in photocurrent generation, thus validating the resistance values extracted from the fit. At the same time, we can establish that the major resistive contribution to the photocurrent generation is given by R_2, the resistance associated with the transport through the space charge layer, which closely matches the dI/dV curve in all the explored potential range.

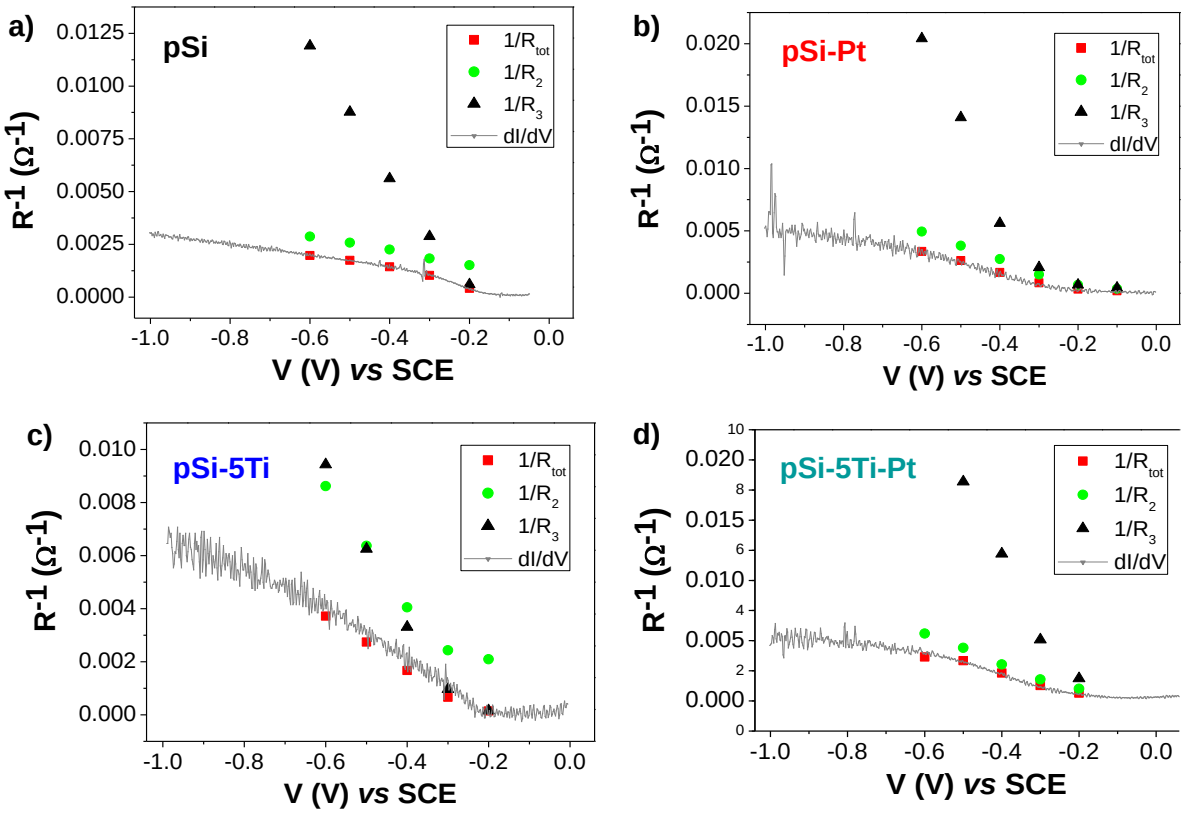

Figure 6. Applied bias dependence of R_{tot}^{-1} (red squares), R_2^{-1} (green circles) and R_3^{-1} (black triangles) for pSi (a), pSi-Pt (b), pSi-5Ti (c) and pSi-5Ti-Pt (d) photocathodes. The resistance values are obtained from the fitting of the EIS data with the equivalent circuit reported in Scheme 1. The corresponding derivative of the I-V curve (dI/dV, not normalized for the area of the electrodes) is reported as a gray solid line.

Figure 7a reports the comparison between R_2^{-1} of all the investigated photocathodes (normalized for the active area of each electrode) as a function of the applied bias, evidencing that both the Pt functionalization and, to a minor extent, the presence of the Ti layer, led to a reduction of R_2 resistance. This is probably due to surface dipole effects caused by the formation of a heterointerface possibly incorporating electron withdrawing centers (such as Ti(IV) and Ti(III) resulting from Ti oxidation, and/or Pt(IV) from H_2PtCl_6), which may favor electron extraction from illuminated silicon. On the other hand, the study of the charge transfer resistance for proton reduction (R_3) evidences the expected lower values in the

presence of the Pt-functionalized substrates (due to better kinetics), with the best results achieved in the case of pSi-5Ti-Pt photocathodes (see Figure 7b).

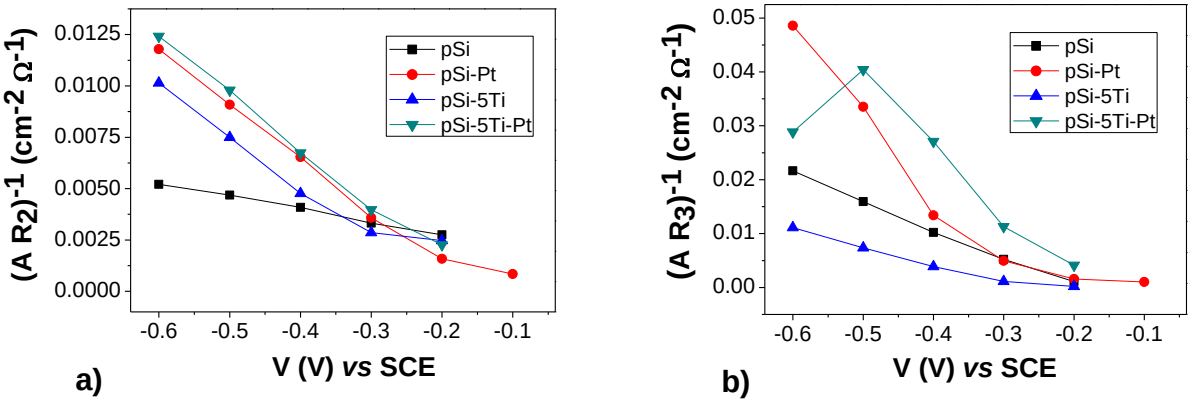

Figure 7. Applied bias dependence of $(AR_2)^{-1}$ (a) and $(AR_3)^{-1}$ (b) for pSi (black squares), pSi-Pt (red circles), pSi-5Ti (blue triangles) and pSi-5Ti-Pt (cyan reversed triangles) photocathodes. The R_2 and R_3 values are obtained from the fitting of the EIS data with the equivalent circuit reported in Scheme 1, and normalized for the area (A) of the electrodes.

From the same fits, the values of the CPE_2 and CPE_3 capacitances, respectively associated to the accumulated charges at the space charge layer and at the photocathode/electrolyte interface (see Scheme 1), can be extracted. The resulting values rank, as expected, in the typical orders of magnitude of depletion and Helmholtz layers of non-porous electrodes, being respectively in the 10^{-8}-10^{-7} F range for CPE_2 and 10^{-6}-10^{-5} F for CPE_3.

In order to provide further insights on a possible role of Ti as doping agent, Mott-Schottky plots have been considered, by examining three different frequency values (respectively in 9165-5456 Hz range for pSi, pSi-Pt and pSi-5Ti, and in 10179-5038 Hz range for pSi-5Ti-Pt) in the dark. In these conditions, the frequency response originated by the capacitance of the Helmholtz layer (CPE_3) is negligible, thus the measured capacitance values result just from the charge accumulated at the depletion layer (CPE_2). This assignation is further confirmed by the corresponding Bode plots, which display a single phase angle peaking at *ca.* 5 kHz for pSi and pSi-5Ti and at *ca.* 50 kHz for pSi-Pt and pSi-5Ti-Pt (Figure S6). Figure 8 shows that a linear behavior is observed in the Mott-Schottky plots when the applied bias ranges from -0.1 to -0.4 V. From the linear fit of these data, we can extrapolate both the flat band potential (V_{FB}, from the intercept with the x-axis) and the acceptors' density (N_a, from the slope), according to equation 1:

$$\frac{A^2}{C^2} = \frac{-2}{\varepsilon_0 \varepsilon\, e\, N_a}\left(V - V_{FB} + \frac{kT}{e}\right)$$

Equation 1 – adapted from [29], see Figure 8.

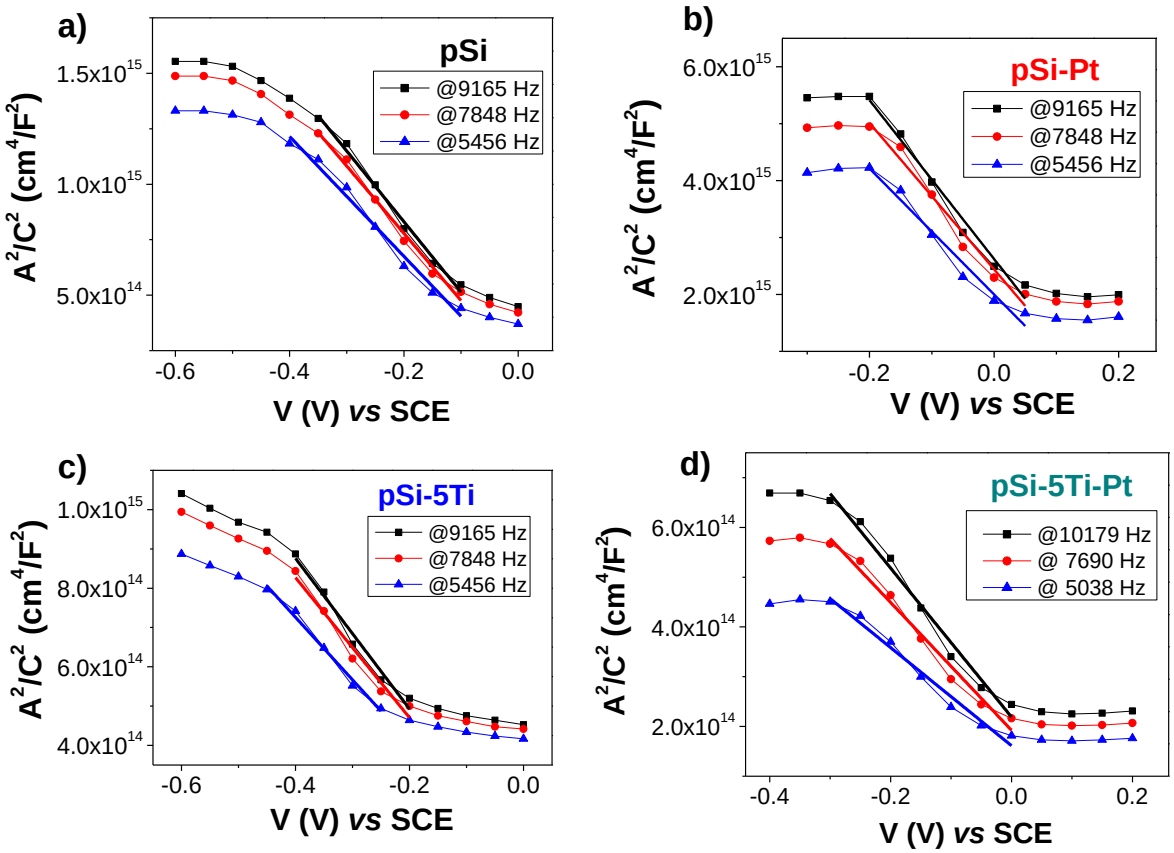

Figure 8. Mott-Schottky plots for pSi (a), pSi-Pt (b), pSi-5Ti (c) and pSi-5Ti-Pt (d) photocathodes recorded in degassed 1 M H_2SO_4 in the dark. Capacitance values at three different frequencies are given.

In particular, we have coherently individuated the photocathodes' flat band potential with essentially no frequency dispersion, obtaining V_{FB} = +0.08 V for both pSi and pSi-5Ti, while in the case of the Pt-functionalized electrodes the V_{FB} is, as expected, *ca.* 100 mV higher (+0.21 V for pSi-Pt and +0.18 V for pSi-5Ti-Pt). These values are in agreement with the corresponding photocurrent onset trend observed in J-V measurements (see Figure 4 and S1) and lie, as expected for a p-type material, quite close to the valence band edge. The slopes calculated for the four photocathodes (inversely proportional to the acceptors' density, N_a) are only slightly different from one another, varying in the order pSi-Pt (1.3×10^{16} cm^4 F^{-2} V^{-1}) > pSi (3.0×10^{15} cm^4 F^{-2} V^{-1}) > pSi-5Ti (1.7×10^{15} cm^4 F^{-2} V^{-1}) ~ pSi-5Ti-Pt (1.3×10^{15} cm^4 F^{-2} V^{-1}). These differences account pretty well for the different dielectric constants of Pt (*ca.* 7, [30]) and TiO_2 (*ca.* 32, [31]) present at the surface of the modified electrodes, thus ruling out any significant doping effect directly influencing the depletion width and the resulting charge extraction. Hence, we can reasonably assume that the density of acceptors (calculated to be *ca.* 4×10^{15} cm^{-3} for bare pSi) does not vary upon Ti-/Pt-functionalization, as well as the resulting depletion layer width. In particular, the latter (w_{dl}) results to be of *ca.* 500 nm at -0.7 V (the photocurrent saturation potential for pSi-5Ti-Pt), and reduces to *ca.* 340 nm at the photocurrent onset, as calculated using equation 2:

$$w_{dl} = \sqrt{\frac{2\,\varepsilon_0\,\varepsilon}{e\,N_a}\left(|V - V_{FB}| + \frac{kT}{e}\right)}$$

Equation 2 – adapted from [8].

The presence of the ultra-thin Ti layer, which is predominantly oxidized to TiO_2, allows for a denser surface coverage of roughly spherical Pt nanoparticles with respect to unmodified pSi, as evidenced by AFM (see Figure 9 and S7). At the same time, the diameter of the Pt clusters formed on pSi is of *ca.* 140 nm, while smaller particles (of 70-90 nm) are deposited on pSi-5Ti surface. Those observations are consistent with the hydrophilic nature of TiO_2, allowing for improved wettability of the surface by the aqueous electrolyte in which Pt electrodeposition is carried out and, possibly, for a preferred adhesion of platinum to TiO_2 with respect to the unmodified silicon surface. Indeed, the total charge passed during the Pt electrodeposition on both pSi and pSi-5Ti photoelectrodes is higher in the case of the Ti-protected surfaces (see Figure S8), supporting the beneficial hydrophilicity of TiO_2 with respect to the recently etched pSi. However, the observed differences in the total charge does not completely account for the different coverage evidenced by AFM measurements. We cannot, thus, rule out the detachment of Pt-NPs due to their non-ideal adhesion to the less hydrophilic pSi surface during electrodeposition or during the rinsing process that follows Pt electrodeposition. Furthermore, given that the calculated space charge width is of the same order of magnitude of the Pt-NPs size (see above), we can reasonably rule out any significant pinch-off effect in the Pt-functionalized photocathodes.

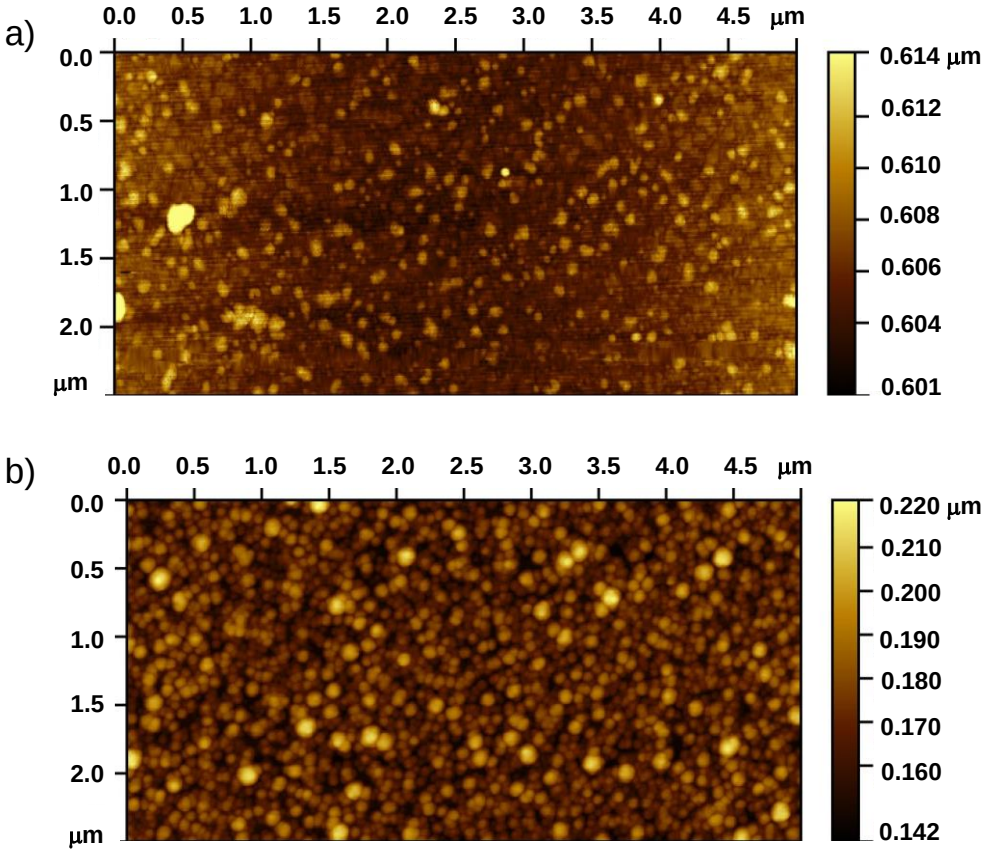

Figure 9. AFM images of pSi-Pt (a) and pSi-5Ti-Pt (b) photocathodes. Pt clusters appear as roughly spherical particles having a diameter of *ca.* 140 nm and 70-90 nm on pSi and pSi-5Ti respectively.

To summarize, the introduction of an ultra-thin Ti/TiO_2 layer leads to an improvement of the photocathodic performances of pSi through two main effects: (i) it enhances charge extraction from the p-type semiconductor, ostensibly through surface dipole or Ti/TiO_2 mediated downhill electron transfer (see also Figure 1); (ii) it allows for a denser surface coverage of smaller Pt nanoparticles.

All this given, pSi-5Ti-Pt shows the best catalytic capabilities within the explored series, consistently leading to the lowest interfacial charge transfer resistance for hydrogen evolution.

4. Conclusions

In this work we have fabricated and characterized PEC photocathodes consisting of p-type silicon coated with Ti-based ultra-thin (5 nm) layers. These layers, obtained by Joule effect evaporation of a metallic Ti target, show a compact morphology conformal with the underlying pSi substrate, as investigated by SEM. XPS analysis reveals a composition consisting mostly of TiO_2, along with a minor fraction of metallic Ti and partially oxidized material (Ti_2O_3). The coatings result effective in both preventing pSi passivation by surface oxidation to SiO_2 (a major issue limiting the use of Si as a photoelectrode material in PEC application), and providing a robust platform for surface functionalization with co-catalysts, as probed by the electrodeposition of Pt-NPs as hydrogen evolving catalysts. The deposition of the ultra-thin titanium film partly attenuates the reflectivity of the photoelectrode surface, but other effects concur to explain the gain in photocathode performances. The best performing electrodes, pSi-5Ti-Pt, show a 200 mV photocurrent onset shift in 1 M H_2SO_4, as well as doubled saturation photocurrent values at -1 V *vs* SCE. Based on photoconversion efficiencies and EIS data, we ascribe this effect to (i) improved extraction of photogenerated charges by the Ti-layer, and (ii) improved surface coverage of Pt NPs on the partially oxidized Ti surfaces, which represent a better substrate for the NPs electrodeposition. Considering the facility of fabrication by Joule effect evaporation, a well-established technique in coating industry, these results provide a general strategy which can be readily extended to other photoelectrode materials suffering from passivation, photocorrosion and/or poor catalytic performance. A further step along this direction would be to investigate the effectiveness of Ti-based ultra-thin coatings also on micro/nano-structured surfaces, where the conformal morphology is likely of critical importance. Preliminary experiments are currently under way in our laboratories.

Funding sources

The project leading to this application has received funding from the European Union's Horizon 2020 research and innovation programme under the Marie Skłodowska-Curie Grant Agreement No 705723. R. Fernandes and N. Patel acknowledge UGC for providing financial support through Dr. DS Kothari, Postdoctoral Fellowship Program and Faculty Recharge Program, respectively.

Appendix A. Supplementary data

The following material is supplied as a supplementary data file: J-V curves recorded under shuttered illumination, reflectance spectra, H_2 evolution traces, APCEs, Nyquist and Bode plots, tabulated resistance values, AFM images and plots of total charge/time during Pt-electrodeposition.

References

[1] V. Balzani, A. Credi, M. Venturi, Photochemical conversion of solar energy, ChemSusChem, 1 (2008) 26-58.
[2] P.V. Kamat, J. Bisquert, Solar Fuels. Photocatalytic Hydrogen Generation, The Journal of Physical Chemistry C, 117 (2013) 14873-14875.
[3] Y. Tachibana, L. Vayssieres, J.R. Durrant, Artificial photosynthesis for solar water-splitting, Nature Photonics, 6 (2012) 511.
[4] S.N. Habisreutinger, L. Schmidt-Mende, J.K. Stolarczyk, Photocatalytic Reduction of CO2 on TiO2 and Other Semiconductors, Angewandte Chemie International Edition, 52 (2013) 7372-7408.

[5] T. Arai, S. Sato, T. Kajino, T. Morikawa, Solar CO2 reduction using H2O by a semiconductor/metal-complex hybrid photocatalyst: enhanced efficiency and demonstration of a wireless system using SrTiO3 photoanodes, Energy & Environmental Science, 6 (2013) 1274-1282.
[6] G. Sahara, H. Kumagai, K. Maeda, N. Kaeffer, V. Artero, M. Higashi, R. Abe, O. Ishitani, Photoelectrochemical Reduction of CO2 Coupled to Water Oxidation Using a Photocathode with a Ru(II)–Re(I) Complex Photocatalyst and a CoOx/TaON Photoanode, Journal of the American Chemical Society, 138 (2016) 14152-14158.
[7] N.S. Lewis, Developing a scalable artificial photosynthesis technology through nanomaterials by design, Nat Nano, 11 (2016) 1010-1019.
[8] R. van de Krol, Principles of Photoelectrochemical Cells, in: R. van de Krol, M. Grätzel (Eds.) Photoelectrochemical Hydrogen Production, Springer US, Boston, MA, 2012, pp. 13-67.
[9] I.E. Castelli, D.D. Landis, K.S. Thygesen, S. Dahl, I. Chorkendorff, T.F. Jaramillo, K.W. Jacobsen, New cubic perovskites for one- and two-photon water splitting using the computational materials repository, Energy & Environmental Science, 5 (2012) 9034-9043.
[10] P.C.K. Vesborg, T.F. Jaramillo, Addressing the terawatt challenge: scalability in the supply of chemical elements for renewable energy, RSC Advances, 2 (2012) 7933.
[11] Y. Hou, B.L. Abrams, P.C.K. Vesborg, M.E. Björketun, K. Herbst, L. Bech, A.M. Setti, C.D. Damsgaard, T. Pedersen, O. Hansen, J. Rossmeisl, S. Dahl, J.K. Nørskov, I. Chorkendorff, Bioinspired molecular co-catalysts bonded to a silicon photocathode for solar hydrogen evolution, Nat Mater, 10 (2011) 434-438.
[12] P.A. Nikolaychuk, The Revised Pourbaix Diagram for Silicon, Silicon, 6 (2014) 109-116.
[13] S.W. Boettcher, E.L. Warren, M.C. Putnam, E.A. Santori, D. Turner-Evans, M.D. Kelzenberg, M.G. Walter, J.R. McKone, B.S. Brunschwig, H.A. Atwater, N.S. Lewis, Photoelectrochemical hydrogen evolution using Si microwire arrays, Journal of the American Chemical Society, 133 (2011) 1216-1219.
[14] B. Seger, A.B. Laursen, P.C.K. Vesborg, T. Pedersen, O. Hansen, S. Dahl, I. Chorkendorff, Hydrogen Production Using a Molybdenum Sulfide Catalyst on a Titanium-Protected n+p-Silicon Photocathode, Angewandte Chemie International Edition, 51 (2012) 9128-9131.
[15] B. Seger, T. Pedersen, A.B. Laursen, P.C.K. Vesborg, O. Hansen, I. Chorkendorff, Using TiO2 as a Conductive Protective Layer for Photocathodic H2 Evolution, Journal of the American Chemical Society, 135 (2013) 1057-1064.
[16] D. Bae, B. Seger, P.C.K. Vesborg, O. Hansen, I. Chorkendorff, Strategies for stable water splitting via protected photoelectrodes, Chemical Society reviews, 46 (2017) 1933-1954.
[17] Z. Huang, J.R. McKone, C. Xiang, R.L. Grimm, E.L. Warren, J.M. Spurgeon, H.-J. Lewerenz, B.S. Brunschwig, N.S. Lewis, Comparison between the measured and modeled hydrogen-evolution activity of Ni- or Pt-coated silicon photocathodes, International Journal of Hydrogen Energy, 39 (2014) 16220-16226.
[18] J.R. McKone, E.L. Warren, M.J. Bierman, S.W. Boettcher, B.S. Brunschwig, N.S. Lewis, H.B. Gray, Evaluation of Pt, Ni, and Ni-Mo electrocatalysts for hydrogen evolution on crystalline Si electrodes, Energy & Environmental Science, 4 (2011) 3573-3583.
[19] Y. Chen, P.D. Tran, P. Boix, Y. Ren, S.Y. Chiam, Z. Li, K. Fu, L.H. Wong, J. Barber, Silicon Decorated with Amorphous Cobalt Molybdenum Sulfide Catalyst as an Efficient Photocathode for Solar Hydrogen Generation, ACS Nano, 9 (2015) 3829-3836.
[20] J. Zhao, L. Cai, H. Li, X. Shi, X. Zheng, Stabilizing Silicon Photocathodes by Solution-Deposited Ni–Fe Layered Double Hydroxide for Efficient Hydrogen Evolution in Alkaline Media, ACS Energy Letters, 2 (2017) 1939-1946.
[21] X.-Q. Bao, M. Fatima Cerqueira, P. Alpuim, L. Liu, Silicon nanowire arrays coupled with cobalt phosphide spheres as low-cost photocathodes for efficient solar hydrogen evolution, Chemical communications, 51 (2015) 10742-10745.
[22] H. Zhang, Q. Ding, D. He, H. Liu, W. Liu, Z. Li, B. Yang, X. Zhang, L. Lei, S. Jin, A p-Si/NiCoSex core/shell nanopillar array photocathode for enhanced photoelectrochemical hydrogen production, Energy & Environmental Science, 9 (2016) 3113-3119.
[23] M.G. Mali, H. Yoon, B.N. Joshi, H. Park, S.S. Al-Deyab, D.C. Lim, S. Ahn, C. Nervi, S.S. Yoon, Enhanced Photoelectrochemical Solar Water Splitting Using a Platinum-Decorated CIGS/CdS/ZnO Photocathode, ACS applied materials & interfaces, 7 (2015) 21619-21625.

[24] NIST X-ray Photoelectron Spectroscopy Database, http://srdata.nist.gov/xps/ National Institute of Standards and Technology, Gaithersburg, 2012.
[25] T. Ohtsuka, M. Masuda, N. Sato, Ellipsometric Study of Anodic Oxide Films on Titanium in Hydrochloric Acid, Sulfuric Acid, and Phosphate Solution, Journal of The Electrochemical Society, 132 (1985) 787-792.
[26] C. Ros, T. Andreu, M.D. Hernández-Alonso, G. Penelas-Pérez, J. Arbiol, J.R. Morante, Charge Transfer Characterization of ALD-Grown TiO2 Protective Layers in Silicon Photocathodes, ACS applied materials & interfaces, 9 (2017) 17932-17941.
[27] S.M.M. Bhola, Brajendra, Effect of pH on the Electrochemical Properties of Oxides formed over β – Ti-15Mo and Mixed Ti-6Al-4V Alloys, International Journal of Electrochemcal Science, 8 (2013) 7075-7087.
[28] D.V. Esposito, I. Levin, T.P. Moffat, A.A. Talin, H2 evolution at Si-based metal–insulator–semiconductor photoelectrodes enhanced by inversion channel charge collection and H spillover, Nature Materials, 12 (2013) 562.
[29] A. Lasia, Semiconductors and Mott-Schottky Plots, Electrochemical Impedance Spectroscopy and its Applications, Springer New York, New York, NY, 2014, pp. 251-255.
[30] A.D. Rakić, A.B. Djurišić, J.M. Elazar, M.L. Majewski, Optical properties of metallic films for vertical-cavity optoelectronic devices, Appl. Opt., 37 (1998) 5271-5283.
[31] S. Swaminathan, P.C. McIntyre, Titania/Alumina Bilayer Gate Dielectrics for Ge MOS Devices: Frequency- and Temperature-Dependent Electrical Characteristics, Electrochemical and Solid-State Letters, 13 (2010) G79-G82.